Application of Neural Networks for Sea Ice Classification in Polarimetric SAR Images

Yoshihisa Hara, *Member, IEEE*, Robert G. Atkins, *Member, IEEE*, Robert T. Shin, *Senior Member, IEEE*, Jin Au Kong, *Fellow, IEEE*, Simon H. Yueh, and Ronald Kwok, *Member, IEEE*

Abstract— **Classification of sea ice types using polarimetric radar is an area of considerable current interest and research. Several automatic methods have been developed to classify sea ice types from fully polarimetric synthetic aperture radar (SAR) images, and these techniques are generally grouped into supervised and unsupervised approaches. In previous work, supervised methods have been shown to yield higher accuracy than unsupervised techniques, but suffer from the need for human interaction to determine classes and training regions. In contrast, unsupervised methods determine classes automatically, but generally show limited ability to accurately divide terrain into natural classes. In this paper, a new classification technique is applied to determine sea ice types in polarimetric and multifrequency SAR images, utilizing an unsupervised neural network to provide automatic classification, and employing an iterative algorithm to improve the performance. The Learning Vector Quantization (LVQ) is first applied to the unsupervised classification of SAR images, and the results are compared with those of a conventional technique, the Migrating Means method. Results show that LVQ outperforms the Migrating Means method, but performance is still poor. An iterative algorithm is then applied where the SAR image is reclassified using the Maximum Likelihood (ML) classifier. It is shown that this algorithm converges, and significantly improves classification accuracy. The new algorithm successfully identifies first-year and multiyear sea ice regions in the images at three frequencies. The results show that L- and P-band images have similar characteristics, while the C-band image is substantially different. Classification based on single features is also carried out using LVQ and the iterative ML method. It is found that the fully polarimetric classification provides a higher accuracy than those based on a single feature. The significance of multilook classification is demonstrated by comparing the results obtained using four-look and single-look classifications. The results show the effect of multilook classification on reducing the speckle in the classified image.**

Manuscript received November 4, 1993; revised February 28, 1995. This work was supported in part by NASA under contracts 958461 and NAGW-1617, in part by the Office of Naval Research under contract N00014-89-J-1107, in part by the U.S. Army/Cold Regions Research & Engineering Laboratory under contract DACA89-90-K-0016; and in part by the Mitsubishi Electric Corporation.

Y. Hara was formerly with the Department of Electrical Engineering and Computer Science and Research Laboratory of Electronics, Massachusetts Institute of Technology, Cambridge, MA 01239. He is now with Mitsubishi Electric Corporation, 325 Kamimachiya, Kamakura, 247 Japan.

R. G. Atkins was formerly with the Department of Electrical Engineering and Computer Science and Research Laboratory of Electronics, Massachusetts Institute of Technology, Cambridge, MA 01239 USA. He is now with the Lincoln Laboratory, Massachusetts Institute of Technology, Cambride, MA 02139 USA.

R. T. Shin and J. A. Kong are with the Department of Electrical Engineering and Computer Science and Research Laboratory of Electronics, Massachusetts Institute of Technology, Cambridge, MA 01239 USA.

S. H. Yueh and R. Kwok are with the Jet Propulsion Laboratory, California Institute of Technology, Pasadena, CA 91109 USA.

IEEE Log Number 9411250.

I. Introduction

SEA ice covers a significant percentage of the ocean surface, including many areas of special interest to a variety of groups. Monitoring the spatial and temporal variations of sea ice is important to industries involved in the exploration for and transportation of mineral and petroleum resources in the polar regions. Military vessels navigating in polar seas are likely to be safer if they have access to information about the thickness of the ice they will encounter and the dynamics of that ice on both short and long term bases. In addition, the scientific community is interested in mapping the distribution of sea ice and sensing its properties because of its influence in ocean/atmosphere heat exchange [1].

The use of microwave frequencies in the remote sensing of sea ice is extremely useful, because it is unaffected by meteorological conditions encountered in the polar regions. The maximum ice extent occurs during the local winter period when solar illumination is severly limited, thus, making optical sensors at best marginally useful. In addition, in the summer season, haze cover is fairly common. These factors make microwave SAR image classification very important for many applications [1].

There have been a number of attempts to measure the scattering properties of sea ice and devise approaches to classify sea ice data. In particular, during the 1989 Coordinated Eastern Arctic Experiment (CEAREX) and pre-ERS-1 Seasonal Ice Zone Experiment (SIZEX 89), a variety of data was collected using polarimetric SAR, and this data was analyzed by numerous groups [3]–[5].

Currently the interpretation of sea ice images is based on experience acquired by the image interpreters, and, to a lesser degree, on experimental measurements and theoretical results. The availability of automatic image classification algorithms, however, would reduce the reliance on manual photo interpretation, and would improve the consistency of such work.

Image classification algorithms are often grouped into supervised and unsupervised approaches. For quantitative analyses of remote sensing data, it is the former which has found more frequent use and yielded higher accuracy (shown when applied to SAR images of the San Francisco Bay area [2]). Examples of supervised classification include Maximum Likelihood (ML) and the minimum distance classifiers [6], [7], both of which have been applied to single feature (e.g. total power, $|HH^2|$, $|VV^2|$ etc.) and polarimetric or multifrequency imagery obtained from radar and optical sensors. These supervised algorithms train the classifier using measured exemplars for

extraction of estimates of relevant statistics or parameters for each class. As such, it is difficult to achieve real-time or automatic operation with supervised classifiers, since operator intervention is required to supply the number and characteristics of the classes, or to designate training regions of known sea ice type from which the characteristics of each class may be determined.

In contrast, unsupervised classification requires no specification of training regions, and automatically classifies the images using algorithms which utilize only the information contained in the measured data itself. Classification is accomplished by identifying clusters of the measured feature vectors, and by designating each distinct cluster as a new class. This automatic operation makes unsupervised classifiers preferable in many applications, particularly those in which real time processing is required. The Migrating Means clustering method (also known as the ISODATA method) is a popular unsupervised scheme [8], and has been applied to many images obtained by optical or infrared sensors. Its use in sea ice classification, however, has been mainly as a preprocessor to supervised classification techniques, reducing the requirements on the image analyst. In addition, for microwave images, only a few examples of unsupervised methods have been reported and these did not use purely statistical methods, but instead employed knowledge of the scattering properties of the terrain. References [9], [10] compared the polarization state of the received wave to that of the transmitted wave in order to deduce the properties of the scatterer, and classified polarimetric SAR images based on the general properties of the Stokes parameters. The performance of these unsupervised algorithms was good in some regions, but unsatisfactory overall.

One alternative to the above conventional methods is a group of classifiers based on the use of neural networks, which has recently received considerable interest [11]. For a number of classification problems, neural networks have been applied and compared to conventional classifiers, and the results have shown that the accuracy of the neural network approach is equivalent to or slightly better than conventional methods. Multilayer Perceptron and conventional classifiers were compared [12]-[14] in the problem of image classification. In all of these applications, neural networks have shown advantages over conventional techniques but as with the conventional classifiers, supervised neural network approaches have outperformed unsupervised methods, and, thus, the former have been more extensively studied. Because of the advantages of unsupervised techniques in automatic and real-time classification, it is of interest to further improve unsupervised neural network classifiers, and to overcome their shortcomings in sea ice classification applications.

In this paper, an unsupervised neural network method is applied to the classification of polarimetric SAR data of sea ice. The characteristics of the sea ice data used in this paper are first discussed briefly. A description of both the conventional and neural network unsupervised classification algorithms is also given. The unsupervised methods of Migrating Means and LVQ are then applied to the sea ice image. LVQ is shown to have better performance than the Migrating Means method, but the performance of both is unsatisfactory. To overcome this poor performance, an iterative method, whereby the image is first classified by an unsupervised neural network and then reclassified by the ML method, is introduced, and applied to the sea ice data. It is shown that this algorithm provides superior performance when compared with stand alone unsupervised neural network classifiers, while preserving the advantages inherent in the automatic operation of unsupervised algorithms. The classified images at three frequencies are then analyzed from physical and mathematical viewpoints using the polarimetric statistics of the sea ice images. Single feature classifications are examined and the results are compared with those obtained by fully polarimetric classification. The effects of multilook classification on the reduction of speckle effects are also demonstrated by comparing the results obtained using four-look and single-look classifications.

II. Conventional Sea Ice Classification

A. Sea Ice Data

In terms of development, sea ice can be roughly categorized into five types: new ice, nilas, young ice, first-year (**FY**) ice, and old ice or multiyear (**MY**) ice. The first three types are usually less than 30 cm in thickness and represent different stages of development of sea ice into first-year ice. After the formation of these thin ice types, the ice is subject to temperature changes, compressive and shearing forces, surface currents, and wind shear. These factors result in significant structural changes, such as ridge formation, breaking, and changes in thickness and surface roughness, which modifies radar return significantly [1].

FY ice has thickness in the range 30 cm–2 m. In contrast, **MY** ice, which by definition has survived at least one summer season, has a typical thickness of more than 2 m. These thicknesses are comparable to the penetration depths at microwave frequencies, so it is effective to use multifrequency radar for observing sea ice at different depths [1].

The image used in this paper is from the Beaufort sea, and the data was collected simultaneously at C-, L-, and P-bands (5.4, 1.25, and 0.4 GHz) by the multifrequency multipolarization SAR installed on the NASA/JPL DC-8 aircraft [5]. This image was acquired in March 1988, during which Arctic winter conditions prevailed in the Beaufort Sea. A mixture of FY and MY ice of various ages can be observed in the image. Under these weather conditions, almost no open water and thin ice are apparent. As a result the following investigations have been limited to classification of two or three types of ice. The original image contains 781 pixels in the range direction, and 4096 in cross range, and the resolution of each pixel is approximately 3 meter in azimuth (single look) and 6.6 meter in slant range. Only one quarter in azimuth direction of the image is processed for the classification, and, thus, the size of the processed image is approximately 5 km in range and 3 km in azimuth. The measurements are fully polarimetric resulting in 5 real quantities for each data sample (magnitudes of HH, VV, and HV, and the relative phases of VV and HV with respect to HH) at each frequency.

B. Conventional Unsupervised Classification Algorithm

Unsupervised classifiers do not rely on training data for each class, but instead attempt to group the data set into classes which exhibit similar behavior in the multidimensional space of the observed feature vector. These methods are often referred to as clustering analysis. Because unsupervised classification utilizes very little *a priori* information or specific physical characteristics of the data, it generally yields poorer performance than supervised methods. It is often preferable, however, because it can operate automatically, exhibits faster processing speed, and does not require the specification of information which may not be readily available.

A common widely used unsupervised technique is the Migrating Means method or Isodata algorithm [8]. This technique is an iterative procedure which estimates reasonable cluster centers by moving each pixel from one cluster to another in such a way that a quadratic distance error is reduced at each step. This algorithm has been used for many remotely sensed images and has given fairly satisfactory results [8].

III. Neural Network Classifier

Neural networks are highly parallel networks with coupling between computational elements, or nodes. The resulting structures represent systems composed of many simple processing elements operating in parallel, whose function is determined by network structure, connection weights, and node function. These structures have been investigated in order to simulate human sensors and intelligence.

More recently, neural networks have been applied to a number of image classification problems, including automatic target recognition and multisensor fusion, and have shown considerable success in matching and sometimes exceeding the performance of conventional algorithms for these applications [15].

In this paper, the most successful unsupervised algorithm, LVQ, was utilized to classify sea ice images. LVQ, however, needs modification to adapt it to image segmentation problems, therefore its modification along with its original algorithm is briefly presented here. In addition, to improve the accuracy of unsupervised classification, a new approach utilizing an iterative ML method developed by [2] is described briefly.

A. Modified Learning Vector Quantization (LVQ)

LVQ which was proposed in [16] is an improved version of general vector quantization, and was originally a supervised method. The algorithm uses reference vectors in the hyperspace of the input feature vectors as training classes. Classification is accomplished by adjusting the reference vectors during training, such that boundaries determined by the minimum Euclidean distance from reference vectors separate the feature space into clustered regions. The details of the algorithm can be found in [2].

B. Iterative ML Method

This method uses LVQ to form initial clusters, and then trains the ML classifier using a training data set first classified by the LVQ unsupervised classifier. The process is then repeated iteratively, training a second ML classifier using data classified by first and so on. The ML classifier implicitly assumes gaussian statistics, but the overall method is unsupervised because the mean and covariance information can be obtained automatically from exemplars created by the clustering initially performed by the LVQ classifier.

This algorithm resembles the Migrating Means method in that the statistical measures are calculated iteratively. In the case of the Migrating Means method, mean values are calculated for each class and the Euclidean distance is utilized as a metric for classification. In contrast, however, this new algorithm employs higher order statistics calculating covariance matrices and utilizing the ML distance measure for classification. This algorithm converges in the same way as that of the Migrating Means method. The details of the algorithm can be found in [2].

IV. Application to Sea Ice Imagery

In this section, the conventional neural network and new iterative unsupervised classifiers are applied to sea ice imagery typical of that described in Section II. Three classes were chosen from the image for each frequency band. Because the penetration depth at each frequency is different, it is possible that the separability of the classes of the image can be different at each frequency. The surface and upper layer of ice can be seen from C-band images, while internal ice structures can be discerned in L-band and P-band images. In this case, however, it was found that each image has the same categories of **FY** ice, **MY** ice, and **Boundary** area, although the distribution of the classes in the image are different depending on frequencies. **Boundary** area includes ridges and cracks between **FY** ice and **MY** ice. The areas selected for computing confusion matrices and measuring accuracies for each class are shown in Fig. 1. Homogeneous areas could not be found in the **Boundary** region, hence, the calculated probability of correct classification should be considered only as an indication of the performance of the classifiers and should not be used as a measure of the absolute accuracy. The final evaluation of the achievable accuracies should be evaluated by comparing the classification maps with field measurements which are not available in this case.

To reduce the speckle effects, multilook averaging was applied before classification. The following polarimetric feature vector which can be deduced from the elements of Mueller matrix [17] is used in the following classification processes:

$$\begin{aligned} X = (&|\mathrm{HH}\cdot\mathrm{HH}^*|, |\mathrm{HV}\cdot\mathrm{HV}^*|, |\mathrm{VV}\cdot\mathrm{VV}^*|, \\ &\mathrm{Re}\{\mathrm{HH}\cdot\mathrm{HV}^*\}, \mathrm{Im}\{\mathrm{HH}\cdot\mathrm{HV}^*\}, \\ &\mathrm{Re}\{\mathrm{HH}\cdot\mathrm{VV}^*\}, \mathrm{Im}\{\mathrm{HH}\cdot\mathrm{VV}^*\}, \\ &\mathrm{Re}\{\mathrm{HV}\cdot\mathrm{VV}^*\}, \mathrm{Im}\{\mathrm{HV}\cdot\mathrm{VV}^*\}). \end{aligned} \quad (1)$$

Averaging the above vector over several pixels yields an averaged feature vector. Classification based on the averaged feature vector is referred to as the multilook classification.

Classification is carried out for the data collected at each frequency band and the results are compared with each other.

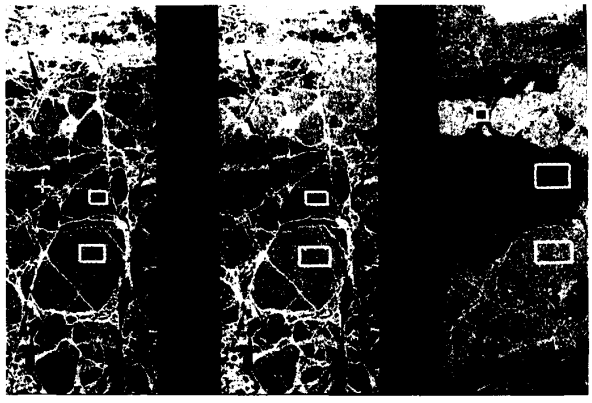

Fig. 1. Testing regions selected from Beaufort sea. From upper box to lower box: MY ice, FY ice, and Boundary region.

TABLE I
CONFUSION MATIRX USING THE MIGRATING MEANS METHOD (C-BAND)

Terrain Class	Migrating Means (C-band)		
	Class 1	Class 2	Class 3
Class 1 (FY)	.997	.003	.000
Class 2 (MY)	.435	.456	.109
Class 3 (BOUNDARY)	.806	.176	.018
Total Accuracy	49.1%		

TABLE II
CONFUSION MATRIX USING THE MIGRATING MEANS METHOD (L- AND P-BAND)

Terrain Class	Migrating Means (L-band)			Migrating Means (P-band)		
	Class 1	Class 2	Class 3	Class 1	Class 2	Class 3
Class 1 (FY)	.011	.989	.000	.000	1.000	.000
Class 2 (MY)	.028	.972	.000	.025	.975	.000
Class 3 (BOUNDARY)	.197	.114	.689	.147	.258	.595
Total Accuracy	55.7%			63.6%		

Classification using all three frequency bands simultaneously is in theory more effective, however, can not be performed here due to the unsatisfactory registration between each of the images.

A. Classification by Migrating Means Method

The Migrating Means method, which has previously been found to be the most effective among conventional methods [2] was first investigated. This algorithm was iterated until the resulting difference of means between successive iterations was less than 0.01. Multilook averaging was employed to stabilize the training procedure and was performed over 512 pixels (32 in azimuth and 16 in range). It was found that approximately 10 iterations were required to obtain convergence. Then in the classification phase, data averaged over every four looks in azimuth were classified. The performance of the Migrating Means method was very poor as shown in the results in Tables I and II for C-, L-, and P-band. Most of the pixels were classified into two classes in the same way as in [2].

TABLE III
CONFUSION MATRIX USING THE LVQ AND ITERATIVE ML METHOD (C-BAND)

Terrain Class	LVQ			LVQ + ML		
	Class 1	Class 2	Class 3	Class 1	Class 2	Class 3
Class 1 (FY)	.808	.000	.192	.948	.001	.051
Class 2 (MY)	.022	.322	.656	.090	.459	.451
Class 3 (BOUNDARY)	.160	.080	.760	.353	.144	.503
Total Accuracy	63.0%			63.6%		

TABLE IV
CONFUSION MATRIX USING THE LVQ AND ITERATIVE ML METHOD (L-BAND)

Terrain Class	LVQ			LVQ + ML		
	Class 1	Class 2	Class 3	Class 1	Class 2	Class 3
Class 1 (FY)	.914	.078	.008	.931	.058	.011
Class 2 (MY)	.505	.481	.014	.478	.472	.050
Class 3 (BOUNDARY)	.028	.122	.850	.022	.122	.856
Total Accuracy	74.8%			75.3%		

TABLE V
CONFUSION MATRIX USING THE LVQ AND ITERATIVE ML METHOD (P-BAND)

Terrain Class	LVQ			LVQ + ML		
	Class 1	Class 2	Class 3	Class 1	Class 2	Class 3
Class 1 (FY)	.994	.006	.000	.961	.039	.000
Class 2 (MY)	.642	.350	.008	.333	.611	.056
Class 3 (BOUNDARY)	.144	.133	.722	.044	.195	.761
Total Accuracy	68.9%			77.8%		

B. Classification by LVQ and Iterative ML Method

Next, LVQ, which was previously found to be the best algorithm for the classification of San Francisco Bay SAR images in [2], was applied. The learning gain was set to 0.005, the same value used in [2], and four-look averaging (in azimuth) was performed before the classification. The results in Tables III–V indicate that LVQ worked much better than the Migrating Means method.

Finally, the iterative ML method was applied to the results of LVQ. Iteration was performed until the resulting difference of the confusion matrix calculated for testing regions between successive iterations was zero, while 15–19 iterations were required to obtain this convergence. The confusion matrices obtained by the iterative ML method for C-, L-, and P-band are shown in Tables III–V, respectively, along with those of LVQ alone. The classified images obtained using LVQ alone and LVQ with the iterative ML method are shown in Figs. 2 and 3. **FY** ice, **MY** ice, and **Boundary** region are color-coded by blue, green, and red, respectively. The images were classified with four-look averaging.

The iterative ML method proved to be particularly effective in the P-band image. The accuracy improved by 8.9% after the iterative method was applied. It is difficult to identify **MY** ice from the original black-and-white image and the image processed by LVQ, but after the iterative ML method is applied, **MY** ice can be easily identified.

In the C-band image, the total accuracy did not change as significantly and it can be seen that a greater number of the pixels in the lower part of the image were correctly classified as **MY** ice. **FY** ice was also classified correctly,

Fig. 2. LVQ classification of Beaufort sea ice Red: Boundary, Green: MY, and Blue: FY (from left to right, P-, L, and C-band images).

Fig. 3. LVQ and iterative ML classification of Beaufort sea ice Red: Boundary, Green: MY, and Blue: FY (from left to right, P-, L-, and C-band images).

and the boundary of each class looks more well-defined after the iteration process. The L-band image does not change very much even after the iterative ML method. It shows that LVQ method worked very well for this case. It should be noted that L-band and P-band images have similar textures after the iteration, although they look very different initially. Considering that the original two images have similar textures, this result shows that the iterative ML method correctly acquired the statistics and converged to a similar point with each image. Note that the upper part of the image was misclassified as **Boundary** region. This error is due to the higher backscatter arising from the small incidence angle in this region. This problem can be corrected by using a normalization technique [10], but it was not implemented here.

By combining images obtained at different frequencies, it is easier to identify each sea ice class. From the classified images, it is seen that the L-band image and the P-band image contain similar information, but there is a large difference in textures between the C-band image and the L- or P-band images. From the C-band image the **MY** ice appears much brighter. Two factors may contribute to this difference of the brightness. One is that **MY** ice has a rougher surface compared to other regions, therefore, leading to a stronger surface scattering. The difference of the roughness between **FY** and **MY** may be so large that even from inspection of the original unclassified image, it is relatively easy to distinguish **FY** and **MY**. However, the **Boundary** region is covered by another layer of ice, and, hence, can not be seen at C-band. The other factor is that **MY** ice has more contribution from volume scattering due to the lower loss in the **MY** ice, which contains more air bubbles and less brine inclusions than the **FY** ice.

In contrast, the L- and P-band images show penetration of the surface. For these frequencies it is difficult to distinguish ice types from the original grey-level of the HH images, but the new algorithm clearly classified them. It is known that **MY** ice floes tend to have more rounded edges and pressure ridges are formed in the lower part of the ice where the ice shears or undergoes compression [1]. These ridges are represented by **Boundary** regions in this experiment. The ridges would act like corner reflectors, resulting in a strong reflection. Note that the texture of ridges in the **FY** ice is found to be finer than that of **MY** ice. In addition, there seems to be one small water region which is not surrounded by **Boundary** region at all in upper left part of the image. This region is classified as **FY** ice in all the images and does not contain any **Boundary** region. However, it was classified as **FY** ice, because the area was too small to merit a fourth class. There are some regions which are classified as **FY** ice or **Boundary** in C-band image, but as **MY** ice in L- and P-band images. It is expected that those are refrozen regions where only the surface of **MY** ice was melted and frozen again. In the refrozen area, the surface would be flat, because it was newly formed, but the internal structure would be the same as **MY** ice.

C. Analysis

The covariance matrix of each class can be analyzed and the way in which each factor contributes to the classification examined. The general form of the polarimetric covariance matrix can be expressed as

$$C_j = \sigma_j \begin{pmatrix} 1 & \beta_j\sqrt{e_j} & \rho_j\sqrt{\gamma_j} \\ \beta_j^*\sqrt{e_j} & e_j & \xi_j\sqrt{e_j\gamma_j} \\ \rho_j^*\sqrt{\gamma_j} & \xi_j^*\sqrt{e_j\gamma_j} & \gamma_j \end{pmatrix} \tag{2}$$

where j represents the class parameters, and

$$\sigma = E[|\mathrm{HH}|^2] \tag{3}$$

$$e = E[|\mathrm{HV}|^2]/\sigma \tag{4}$$

$$\gamma = E[|\mathrm{VV}|^2]/\sigma \tag{5}$$

$$\rho = \frac{E[\mathrm{HH}\cdot\mathrm{VV}^*]}{\sigma\sqrt{\gamma}} \tag{6}$$

$$\beta = \frac{E[\mathrm{HH}\cdot\mathrm{HV}^*]}{\sigma\sqrt{e}} \tag{7}$$

$$\xi = \frac{E[\mathrm{HV}\cdot\mathrm{VV}^*]}{\sigma\sqrt{e\gamma}}. \tag{8}$$

The parameters, ρ, β, and ξ are the complex correlation coefficients between the polarimetric channels, γ is the ratio

TABLE VI
COVARIANCE PARAMETERS (C-BAND)

Covariance Parameter	FY	MY	BOUNDARY
σ (dB)	0.00000	10.17810	5.61046
e	0.05397	0.12326	0.07294
γ	0.79549	1.04454	0.98475
$\lvert\rho\rvert$	0.69414	0.69879	0.73637
ϕ_ρ (deg)	-0.28057	-9.56324	0.77179
$\lvert\beta\rvert$	0.06543	0.06498	0.08336
ϕ_β (deg)	-48.73046	-7.14889	-19.54189
$\lvert\xi\rvert$	0.03980	0.05414	0.07898
ϕ_ξ (deg)	-18.81950	-45.95820	-18.97467

TABLE VII
COVARIANCE PARAMETERS (L-BAND)

Covariance Parameter	FY	MY	BOUNDARY
σ(dB)	0.00000	6.91202	13.10811
e	0.07549	0.08399	0.14530
γ	1.08574	0.97449	0.83611
$\lvert\rho\rvert$	0.70918	0.83200	0.76954
ϕ_ρ (deg)	31.21599	27.79400	19.06039
$\lvert\beta\rvert$	0.54360	0.63981	0.57123
ϕ_β (deg)	-70.90204	-69.12583	-72.89827
$\lvert\xi\rvert$	0.44605	0.57343	0.51568
ϕ_ξ (deg)	98.50699	95.33809	86.91537

TABLE VIII
COVARIANCE PARAMETERS (P-BAND)

Covariance Parameter	FY	MY	BOUNDARY
σ(dB)	0.00000	7.43703	15.81798
e	0.05723	0.02750	0.05148
γ	1.08447	1.02327	0.83956
$\lvert\rho\rvert$	0.76601	0.86343	0.79896
ϕ_ρ (deg)	93.33402	87.83180	77.24619
$\lvert\beta\rvert$	0.07026	0.09553	0.07488
ϕ_β (deg)	106.48116	125.58476	141.52924
$\lvert\xi\rvert$	0.06301	0.09509	0.09034
ϕ_ξ (deg)	-21.30305	-38.95760	-61.52669

of average VV power to the average HH power, and e is the depolarization ratio within the image. These covariance parameters for each class after the iterative ML method are shown in Tables VI–VIII for C-, L-, and P-band, respectively. σ is normalized by its value of the **FY** ice, i.e., σ of the **FY** ice is set to 0 dB.

Covariance parameters of L-band and P-band images are similar, indicating that the scattering from sea ice at L-band and P-band is contributed by similar scattering sources. In the C- and P-band images, the parameters β and ξ are relatively small as expected from sea ice with azimuthally symmetric random inclusions [18]. In the L-band image, those two parameters are large, as perhaps due to the couplings between HH and HV, and VV and HV channels in the radar.

It is noted that the VV return of **MY** ice has almost the same variance as HH at every frequency, while the VV return of **FY** ice has much smaller variance than HH at C-band and the same variance at L- and P-band. This result suggests that **FY** ice has a different feature from **MY** ice at the surface, but has a similar signature as that of **MY** ice at the bottom.

From the covariance matrix, the large difference in σ and the small difference of other parameters among classes indicate that σ would dominate the classification, especially in L- and P-band images. To examine how the σ component contributes to the classification, single feature classification using only σ was performed by the LVQ and iterative ML method. To reduce the speckle effects, four-look averaging was again performed. Hence the Gamma distribution of (9) was assumed for the averaged intensity for the ML classification,

$$p(X|\omega_i) = \frac{1}{\Gamma(N)}\left(\frac{N}{\sigma_i^2}\right)\left(\frac{NX}{\sigma_i^2}\right)^{N-1}\exp\left[-\left(\frac{NX}{\sigma_i^2}\right)\right] \tag{9}$$

where

$$X = \frac{\sum_{n=1}^{N} X_n}{N} \tag{10}$$

and N is the number of looks. The results obtained by single feature classification are shown in Tables IX and X. For L- and P-band images, σ is found to be very important. The accuracy of the single feature classification was only 0.2% less than for L-band image and 3% for P-band image compared to those of fully polarimetric classification. In contrast, the classification accuracy for C-band image was more than 10% worse than that of fully polarimetric case. This result seems to indicate that information other than the intensity is significant in the C-band image. This significance is clear from the processed image shown in Fig. 4. In the image classified by the single-feature, the lower portion of **MY** ice is poorly classified, while in the image classified from the fully polarimetric data, it is correctly classified.

Single feature classifications were also done using other features, $|\mathrm{HV}|^2$ and $|\mathrm{VV}|^2$, to evaluate the contribution of each parameter to the classification. The accuracies of these single feature classifications are summarized in Table XI. For the C- and P-band data, the accuracy using $|\mathrm{HV}|^2$ is poor, and accuracy using $|\mathrm{VV}|^2$ is comparable to that using $|\mathrm{HH}|^2$. At L-band, the correlation between HH and HV is large, hence,

TABLE IX
CONFUSION MATRIX (CLASSIFICATION BASED ON $|\mathrm{HH}|^2$, C-BAND)

Terrain Class	$\lvert HH\rvert^2$ (C-band)		
	Class 1	Class 2	Class 3
Class 1 (FY)	.831	.000	.169
Class 2 (MY)	.250	.301	.449
Class 3 (BOUNDARY)	.422	.137	.441
Total Accuracy	52.4%		

TABLE X
CONFUSION MATRIX (CLASSIFICATION BASED ON $|\mathrm{HH}|^2$, L- AND P-BAND)

Terrain Class	$\lvert HH\rvert^2$ (L-band)			$\lvert HH\rvert^2$ (P-band)		
	Class 1	Class 2	Class 3	Class 1	Class 2	Class 3
Class 1 (FY)	.955	.045	.000	.989	.011	.000
Class 2 (MY)	.382	.515	.143	.376	.540	.084
Class 3 (BOUNDARY)	.031	.185	.784	.054	.230	.716
Total Accuracy	75.1%			74.8%		

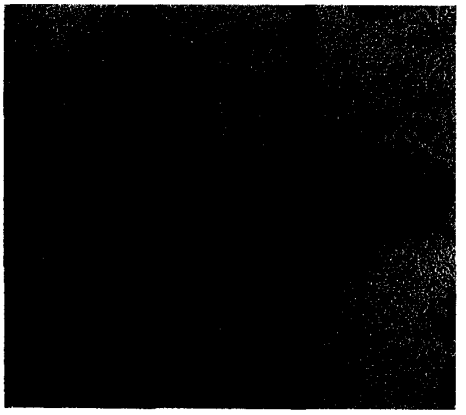

Fig. 4. Single-feature classification of Beaufort sea ice Red: Boundary, Green: MY, and Blue: FY (from left to right, P-, L, and C-band images).

TABLE XI
CLASSIFICATION ACCURACIES BASED ON SINGLE FEATURES

Frequency Band	$\|HH\|^2$	$\|HV\|^2$	$\|VV\|^2$
C-band	52.4%	54.7%	56.1%
L-band	75.1%	71.4%	74.1%
P-band	74.8%	62.5%	72.2%

single feature classification using $|\mathrm{HV}|^2$ performs almost as well as that using $|\mathrm{HH}|^2$.

In addition to covariance parameters, polarization signatures are examined to visualize the scattering characteristics. In measuring the magnitude and phase at four polarization, it is possible to construct the polarization behavior for every resolution element of an image. Figs. 5 and 6 show the polarization signatures of **FY** and **MY** at C-band, which were found to show interesting features.

From Fig. 5, it is shown that there are three small peaks at HH and VV linear copolarized combinations. Each of these small peaks has equivalent power in a uniform rough surface signature. Minimums occur at right- or left-handed circular polarizations, indicating that most of the scattered returns are highly polarized. The fact that the proportion of random or unpolarized waves is small is due to small cross-polarization.

The copolarized signature of **MY** ice shows a different pattern. There is a peak at VV linear copolarization which extends toward HH linear copolarizations. HH power return is relatively lower, but the minimum points again appear at circular polarizations. Note that the absolute pedestal height in the **MY** ice signature is due to the cross-polarization component which may be contributed by the relatively large volume scattering from the air bubbles. It was found that the signature of **Boundary** region also showed similar features as **FY** ice.

D. Effects of Multilook

The effects of multilook averaging on the classifier are examined in this section. To illustrate the effects of multilook averaging, classification based on single look was compared with the results based on four-look averaging, results of which have been shown in the previous sections. The accuracy of

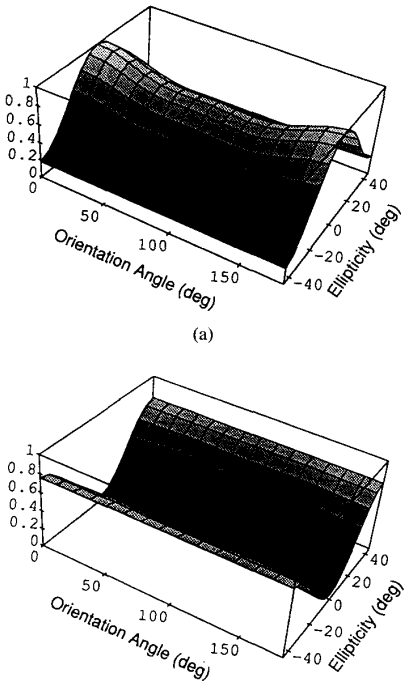

Fig. 5. C-band polarization signature (**FY** ice). (a) Copolarized signature; (b) crosspolarized signature.

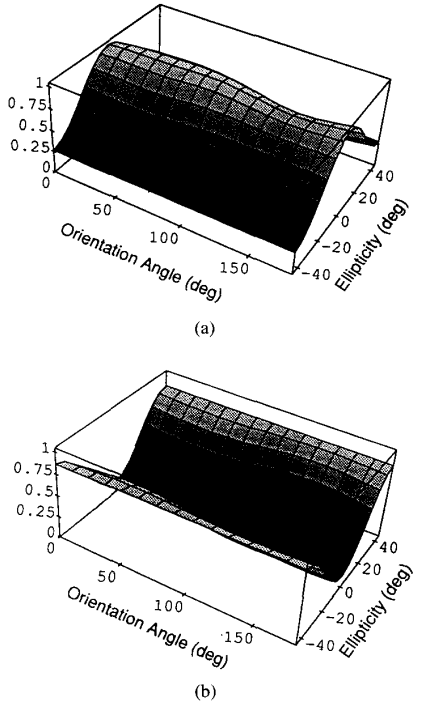

Fig. 6. C-band polarization signature (**MY** ice). (a) Copolarized signature; (b) crosspolarized signature.

TABLE XII
COMPARISON OF ACCURACIES BETWEEN FOUR-LOOK AND SINGLE-LOOK CLASSIFICATIONS

Frequency band	Four look	Single look
C-band	63.6%	63.9%
L-band	75.3%	61.1%
P-band	77.8%	54.6%

Fig. 7. LVQ classification of Beaufort sea ice (with single-look) Red: Boundary, Green: MY, and Blue: FY (from left to right, P-, L, and C-band images).

the classifier with single-look averaging is shown in Table XII along with that with four-look averaging. The single-look images classified by LVQ, and LVQ with the iterative ML method are shown in Figs. 7 and 8. It is clear that the single look method displays very poor performance in the L- and P-band images. Due to the speckle in single look images, it is difficult to identify the **MY** region, especially in the lower part of the image. For the C-band image, the total accuracy did not change as much. But from the processed image it was found that these three classes are clearly more separated in the four-look image than in the single-look image. From this experiment, it was confirmed that four-look averaging is capable of reducing the effects of speckle, and therefore improves the classification accuracy.

V. CONCLUSION

An unsupervised neural network has been described and applied to the classification of sea ice in SAR imagery. LVQ displayed superior performance when compared to the Migrating Means method. To further improve the performance, a new algorithm was introduced which employed LVQ to perform the initial clustering and improved the results by an iterative ML method. This method was seen to improve the performance of the unsupervised LVQ method significantly, while preserving the advantages of automatic operation inherent in unsupervised techniques. The results showed that L- and P-band images have similar characteristics, while the C-band image is substantially different from the lower frequency ones. The upper structures of the sea ice were more obvious in the C-band image, and the internal structures of the sea ice were more prevalent in the L- and P-band images. It was found that the C-band image had the most distinct features separating classes. The factors contributing to the classification were analyzed, and it was found that the dominant feature is the intensity of HH in the L- and P-band images, while fully polarimetric classification helped in the C-band image and gave the optimal result. In addition, it was found that multilook averaging was not only necessary in the training phase, but also in the classification phase, to stabilize the training, and to suppress the misclassification caused by the effects of speckle.

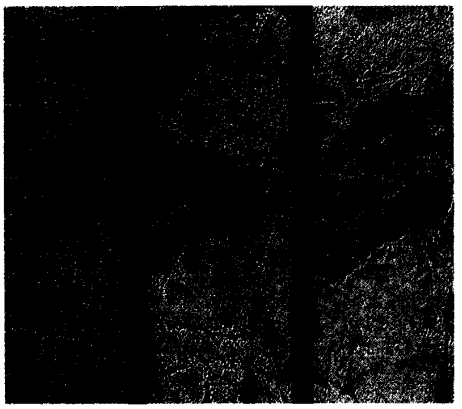

Fig. 8. LVQ and iterative ML classification of Beaufort sea ice (with single-look) Red: Boundary, Green: MY, and Blue: FY (from left to right, P-, L, and C-band images).

REFERENCES

[1] F. T. Ulaby, R. K. Moore, and A. K. Fung, *Microwave Remote Sensing: Volume III*. Norwood, MA: Artech House, 1986.

[2] Y. Hara, R. G. Atkins, S. H. Yueh, R. T. Shin, and J. A. Kong, "Application of neural networks to radar image classification," *IEEE Trans. Geosci. Remote Sensing*, vol. 32, pp. 100–109, 1994.

[3] R. A. Shuchman, L. L. Sutherland, C. C. Wackerman, O. M. Johannessen, J. A. Johannessen, and L. H. Pettersson, "Geophysical information on the winter marginal ice zone obtained from CEAREX SAR data," in *Proc. Int. Geosci. Remote Sensing Symp.*, College Park, MD, May 20–24, 1990, pp. 1505–1508.

[4] P. M. Haugan, O. M. Johannessen, S. Sandven, and R. Preller, "Sea ice modeling in the barents sea During SIZEX 89," in *Proc. Int. Geosci. Remote Sensing Symp.*, College Park, MD, May 20–24, 1990, pp. 1509–1512.

[5] M. R. Drinkwater, R. Kwok, and E. Rignot, "Synthetic aperture radar polarimetry of sea ice," in *Proc. Int. Geosci. Remote Sensing Symp.*, College Park, MD, May 20–24, 1990, pp. 1525–1528.

[6] A. G. Wacker and D. A. Landgrebe, "Minimum distance classification in remote sensing," in *Proc. First Canadian Symp. Remote Sensing*, Ottawa, 1972.

[7] P. H. Swain and S. M. Davis, Eds., *Remote Sensing: The Quantitative Approach*. New York: McGraw-Hill, 1978.

[8] J. A. Richards, *Remote Sensing Digital Image Analysis: An Introduction*. Berlin: Springer-Verlag, 1986.

[9] J. J. van Zyl, "Unsupervised classification of scattering behavior using radar polarimetry data," *IEEE Trans. Geosci. Remote Sensing*, vol. 27, no. 1, pp. 36–45, 1989.

[10] H. H. Lim, A. A. Swartz, H. A. Yueh, J. A. Kong, R. T. Shin, and J. J. van Zyl, "Classification of earth terrain using polarimetric synthetic aperture radar images," *J. Geophys. Research*, vol. 94, no. B6, pp. 7049–7057, June 1989.

[11] P. D. Heerman and N. Khazenie, "Classification of multispectral remote sensing data using a back-propagation neural network," *IEEE Trans. Geosci. Remote Sensing*, vol. 30, pp. 81–88, Jan. 1992.

[12] J. A. Benediktsson, P. H. Swain, and O. K. Ersoy, "Neural network approaches versus statistical methods in classification of multisource

remote sensing data," *IEEE Trans. Geosci. Remote Sensing*, vol. 28, pp. 540–552, July 1990.
[13] S. E. Decatur, "Applications of neural networks to terrain classification," M.S. thesis, Dept. Elec. Eng. Computer Sci., Massachusetts Inst. Tech., Cambridge, June 1989.
[14] J. Orlando, R. Mann, and S. Haykin, "Radar classification of sea-ice using traditional and neural classifiers," in *Proc. Int. Joint Conf. Neural Networks*, Washington, DC, Jan. 15–19, 1990, pp. II-263–266.
[15] F. Sadjadi, "Automatic object recognition: Critical issues and current approaches," *SPIE*, vol. 1471, pp. 303–313, 1991.
[16] T. Kohonen, *Self-Organization and Associative Memory*. Berlin: Springer-Verlag, 1989.
[17] L. Tsang, J. A. Kong, and R. T. Shin, *Theory of Microwave Remote Sensing*. New York: Wiley, 1985.
[18] M. Borgeaud, R. T. Shin, and J. A. Kong, "Theoretical models for polarimetric radar clutter," *J. Electromagnetic Waves Appl.*, vol. 1, no. 1, pp. 67–86, 1987.

Yoshihisa Hara (M'82) was born in Yokohama, Japan, in 1960. He received the B.S. degree in mathematical engineering and information physics from the University of Tokyo, Tokyo, Japan, and the M.S. degree in electrical engineering and computer science from Massachusetts Institute of Technology, Cambridge, in 1983 and 1991, respectively.

Since 1983, he has worked at Mitsubishi Electric Corporation, Japan, on signal processing of radars, especially of SAR, ISAR, and microwave scatterometer. His research interests include radar signal processing, image classification, neural networks, and remote sensing.

Mr. Hara is a member of the Society of Instrument and Control Engineers.

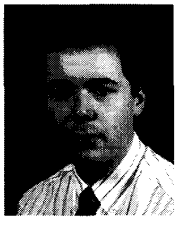

Robert G. Atkins (S'85–M'94) received the B.S., M.S., and Ph.D. degrees in electrical engineering from Massachusetts Institute of Technology, in 1987, 1988, and 1993, respectively

Between 1985 and 1991, he was a Cooperative Student, Summer Staff member, and Research Assistant with MIT Lincoln Laboratory, where he worked on a variety of research projects related to air defense. Since 1993, he has been a member of the Technical Staff of the Air Defense Techniques Group. His research interests include electromagnetic scattering and remote sensing, synthetic aperture radar imaging, and target detection and classification.

Dr. Atkins is currently a member of Eta Kappa Nu, Tau Beta Pi, Sigma Xi, and the Armed Forces Communications and Electronic Association.

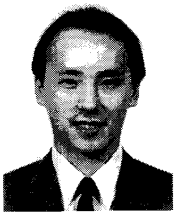

Robert T. Shin (S'82–M'83–SM'90) received the B.S., M.S., and Ph.D. degrees in electrical engineering from Massachusetts Institute of Technology, Cambridge, in 1977, 1980, and 1984, respectively.

Since 1984, he has been a member of the Air Defense Techniques Group at MIT Lincoln Laboratory, as a Senior Staff from 1989 and as an Assistant Group Leader since 1992. He is also the Assistant Director of the Center for Electromagnetic Theory and Applications (CETA) in the Research Laboratory of Electronics at MIT. He is the coauthor of *Theory of Microwave Remote Sensing* (Wiley, 1985). He has published more than 100 refereed journal articles and conference papers and supervised more than 20 theses.

Dr. Shin is a member of the Electromagnetics Academy, American Geophysical Union, Tau Beta Pi, Eta Kappa Nu, and Commission F of the International Union of Radio Science. Since 1987, he has served on the Editorial Board of the Journal of Electromagnetic Waves and Applications.

Jin Au Kong (S'65–M'69–SM'74–F'85), is a Professor of Electrical Engineering at Massachusetts Institute of Technology, Cambridge. His research interest is in the area of electromagnetic wave theory and applications. He has published eight books, including *Electromagnetic Wave Theory* (Wiley), more than 400 refereed articles and book chapters, and supervised more than 120 theses. He is editor-in-chief of the Journal of Electromagnetics Waves and Applications, chief editor of the book series *Progress in Electromagnetics Research*, and editor of the Wiley Series in remote sensing.

Simon H. Yueh, for photograph and biography, please see p. 91 of the January issue of this TRANSACTIONS.

Ronald Kwok (M'86), for photograph and biography, please see p. 400 of the March issue of this TRANSACTIONS.